CrossMark

Direct reforming of biogas on Ni-based SOFC anodes: Modelling of heterogeneous reactions and validation with experiments

Massimo Santarelli [a],*, Francesco Quesito [a], Valerio Novaresio [a], Cosimo Guerra [a], Andrea Lanzini [a], Davide Beretta [b]

[a] Energy Department, Politecnico di Torino, Corso Duca degli Abruzzi 24, 10129 Torino, Italy
[b] Centro Ricerca e Sviluppo, Edison S.p.a, Via La Pira 2, 10028 Trofarello (TO), Italy

HIGHLIGHTS

- Operational maps of a tubular SOFC cell running on direct reforming of biogas.
- Kinetic model of chemical and electrochemical conversion of biogas in solid oxide fuel cells (SOFC).
- Validation of the model through polarization and GC analysis of anode exhaust gas.
- Use of the model to predict and analyze the gas composition along the anode in different geometries and operating conditions.

ARTICLE INFO

ABSTRACT

This work focuses on the heterogeneous reactions taking place in a tubular anode-supported solid oxide fuel cell (SOFC) when the designated fuel is biogas from anaerobic digestion directly feeding the fuel cell. Operational maps of the fuel cell running on direct reforming of biogas were first obtained. Hence a mathematical model incorporating the kinetics of reforming reactions on Ni catalyst was used to predict the gas composition profile along the fuel channel. The model was validated against experimental data based on polarization curves. Also, the anode off-gas composition was collected and analyzed through a gas chromatograph. Finally, the model has been used to predict and analyze the gas composition change along the anode channel to evaluate effectiveness of the direct steam reforming when varying cell temperature, inlet fuel composition and the type of reforming process. The simulations results confirmed that thermodynamic-equilibrium conditions are not fully achieved inside the anode channel. It also outlines that a direct biogas utilization in an anode-supported SOFC is able to provide good performance and to ensure a good conversion of the methane even though when the cell temperature is far from the nominal value.

1. Introduction

As suggested by recent advances in bio-chemical science and technology, biogas from anaerobic digestion is an alternative to conventional fuels for producing electricity in a distributed generation framework [1,2]. Biogas can be produced starting from several wastes that include the organic fraction of municipal solid waste (food waste, mostly), sewage, agricultural (or green) waste (e.g., straw and harvest residues) and animal manure. Industrial and municipal waste-water treatment (WWT) plants – often combined together – and landfills are generally the two largest biogas producers [3].

The typical gas composition includes mostly methane (50–70% vol.) and CO_2 (30–50% vol.), plus some nitrogen ($\sim 1\%$ vol.); Several trace contaminants such as sulfur compounds (including COS and mercaptans), halogens, siloxanes, etc. are also found [3–5]. The high methane content (variable according to the biomass waste/feedstock used, and micro-biological treatments in the digester) of biogas makes it a good substitute of natural gas.

Usually, biogas is burnt in engines to produce mechanical power then converted into electricity; as an alternative, it could be used to feed a solid oxide fuel cells (SOFCs) to generate electricity via a high-efficiency electrochemical conversion process. The SOFC can be safely operated with direct biogas once contaminants are removed, or reduced at acceptable values, in a processing/cleaning

section. Also, a certain oxygen-to-carbon (O/C) ratio (generally above 2) must be provided at the anode inlet to avoid carbon build-up in the Ni-based anode electrode; the oxygen carrier is either H_2O, CO_2, or even O_2, that can be available externally or through the recirculation of a fraction of the anode exhaust (H_2O and CO_2, only) [6–9].

Especially if a direct use of biogas in the SOFC is sought, it becomes important to understand and predict both the chemical processes (heterogeneous catalytic reactions) and electrochemical reactions occurring within the anode volume [10,11] as well as their coupling [12–15]. So far the elementary kinetic steps involved in the electro-oxidation of H_2 and CO in a Ni–YSZ anode have been only partially understood, especially for the CO compound.

In particular, it is interesting to understand for a multi-component fuel mixture containing CH_4, H_2 and CO (as for direct reforming of biogas) — plus an oxygen carrier in the form of CO_2 and steam — which species are actually reacting on the TPB region.

For instance, for H_2–CO mixtures with an high amount of H_2 (>55% was mentioned in the work of Jiang and Virkar [16]), the water gas-shift reaction is considered so fast in a NI–YSZ electrode to prevent the direct electro-oxidation of CO that is rather converted catalytically to H_2. This conversion pathway for CO within an SOFC seems likely also looking at the reported lower kinetics for CO electro-oxidation [16], even though CO electrochemical activity was experimentally verified in a Ni–YSZ SOFC [17,18].

Similar works are present in literature, but usually performed over button cell design. Most of them are focused on detailed 1D studies through the anodic electrodes using simplified electrochemical models [19] or more complex ones [20]. Other works take into account the in-plane flow distribution of bulk species concentrations but only considering hydrogen as a fuel [21].

In this work, a detailed numerical model has been developed, which includes the model developed by Deutschmann et al. [13,14]. The aim of the proposed model is to evaluate the catalytic and electro-catalytic conversion of the fuel (i.e., biogas) in the fuel cell and to predict the anodic gas composition along the fuel channel. In particular, a real tubular commercial available cell was considered (with a higher level of significance compared to a button cell): in fact, the size of the cell implies that bulk species distribution can be taken into account. The model is validated against experimental data obtained for an anode-supported tubular SOFC: in particular, through the monitoring of the anode off-gas composition using a gas chromatograph. In fact, the model focusses to well reproduce the gas conversion due to heterogeneous reactions: the validation considering the outlet species concentration has been preferred compared to the polarization one, which usually is obtained simply by tuning some electrochemical macro-parameters. Also, operational maps of the SOFC were obtained, studying the impact of relevant operational variables (*FU*, fuel composition, steam addition) on cell performance.

2. The SOFC mathematical model

The numerical model was implemented using an in-house code based on Cantera tool [22]. The reforming process occurring inside the anode channel of a tubular anode-supported SOFC (a modified version of our kinetic model for planar cells is also available) was evaluated considering a detailed kinetic mechanics for heterogeneous reactions. Both thermodynamic and electrochemical phenomena are taken into account. The reaction volume (i.e., the anode channel) was discretized both in radial and axial directions. A grid independence analysis was performed by varying the number of nodes in both directions independently. Finally, the grid size was adequately reduced to minimize the computational time while preserving a fast convergence to stable solution.

2.1. Main model assumptions

Considering the peculiar flow characteristics established in a tubular fuel cell, the present model consists of a series of 1D problems along the axial direction. Species conservation is applied between adjacent elements. The whole approach represents an acceptable approximation since the fuel channel typically has a characteristic diameter less than a centimeter and mean velocities less than 1 m s^{-1} that imply the Reynolds number is in the order of hundreds. Very low Mach number and nearly constant pressure guarantee that also boundary conditions satisfy this approach. Hence the flow equations reduce to a set of ordinary differential equations in the radial coordinate.

The species-conservation equations can be written as:

$$\rho \frac{dY_k}{dt} = -\rho u \frac{dY_k}{dr} - \frac{dJ_k}{dr} + W_k \dot{\omega}_k \tag{1}$$

The convective terms were computed using an upwind differencing method, while a central differencing method was employed to compute the diffusive terms. Boundary conditions for species mass flows are set at the inlet (Dirichlet) and at anode/channel interface (Neumann). The fluxes J_k was computed using the mixture-averaged transport model, with the diffusion velocity being composed of three parts:

$$V_k = v_k + w_k + V_c \tag{2}$$

where v_k is the ordinary diffusion velocity and is given in the Curtiss–Hirschfelder [23] approximation by:

$$v_k = D_{km} \frac{1}{X_k} \frac{dX_k}{dx} \tag{3}$$

the mixture-averaged diffusion coefficient D_{km} is given explicitly in terms of the binary diffusion coefficients D_{kj}:

$$D_{km} = \frac{1 - Y_k}{\sum_{j \neq k}^{K} \frac{X_j}{D_{kj}}} \tag{4}$$

A zero thermal diffusion velocity w_k was considered in this preliminary isothermal simulation. The correction velocity V_c was included to insure that the mass fractions sum to unity. The formulation of the correction velocity is the one recommended by Coffee and Heimerl [24] in their extensive investigation of approximate transport models.

The electrochemical oxidation at the anode is attributed to hydrogen only. Once the current density i is set, it is possible to evaluate the molar flux of the gas species involved in the electrochemical reactions as:

$$J_{H_2,a} = -\frac{i}{2F} \tag{5}$$

$$J_{H_2O,a} = \frac{i}{2F} \tag{6}$$

A positive flux at the anode means a net species production.

The molar production rates $\dot{\omega}_k$ are evaluated using a heterogeneous reaction mechanism described in Table 1. The mechanism was taken from reference [25] and manually translated from

Table 1
Heterogeneous reaction mechanism for methane reforming on nickel catalyst.

#	Reaction	A [a]	n	E [a]	$\varepsilon_{CO(s)}$
1	$H_2 + (Ni) + (Ni) \rightarrow H(Ni) + H(Ni)$	$1.000 \cdot 10^{-02}$ [b]	0.0	0.0	–
2	$H(Ni) + H(Ni) \rightarrow H_2 + (Ni) + (Ni)$	$2.545 \cdot 10^{+19}$	0.0	81.2	–
3	$O_2 + (Ni) + (Ni) \rightarrow O(Ni) + O(Ni)$	$1.000 \cdot 10^{-02}$ [b]	0.0	0.0	–
4	$O(Ni) + O(Ni) \rightarrow (Ni) + (Ni) + O_2$	$4.283 \cdot 10^{+23}$	0.0	474.9	–
5	$CH_4 + (Ni) \rightarrow CH_4(Ni)$	$8.000 \cdot 10^{-03}$ [b]	0.0	0.0	–
6	$CH_4(Ni) \rightarrow (Ni) + CH_4$	$8.705 \cdot 10^{+15}$	0.0	37.5	–
7	$H_2O + (Ni) \rightarrow H_2O(Ni)$	$1.000 \cdot 10^{-01}$ [b]	0.0	0.0	–
8	$H_2O(Ni) \rightarrow (Ni) + H_2O$	$3.732 \cdot 10^{+12}$	0.0	60.8	–
9	$CO_2 + (Ni) \rightarrow CO_2(Ni)$	$1.000 \cdot 10^{-05}$ [b]	0.0	0.0	–
10	$CO_2(Ni) \rightarrow (Ni) + CO_2(Ni)$	$6.447 \cdot 10^{+07}$	0.0	26.0	–
11	$CO + (Ni) \rightarrow CO(Ni)$	$5.000 \cdot 10^{-01}$ [b]	0.0	0.0	–
12	$CO(Ni) \rightarrow (Ni) + CO(Ni)$	$3.563 \cdot 10^{+11}$	0.0	111.3	-50.0 [c]
13	$O(Ni) + H(Ni) \rightarrow OH(Ni) + (Ni)$	$5.000 \cdot 10^{+22}$	0.0	97.9	–
14	$OH(Ni) + (Ni) \rightarrow O(Ni) + H(Ni)$	$1.781 \cdot 10^{+21}$	0.0	36.1	–
15	$OH(Ni) + H(Ni) \rightarrow H_2O(Ni) + (Ni)$	$3.000 \cdot 10^{+20}$	0.0	42.7	–
16	$H_2O(Ni) + (Ni) \rightarrow OH(Ni) + H(Ni)$	$2.271 \cdot 10^{+21}$	0.0	91.8	–
17	$OH(Ni) + OH(Ni) \rightarrow O(Ni) + H_2O(Ni)$	$3.000 \cdot 10^{+21}$	0.0	100.0	–
18	$O(Ni) + H_2O(Ni) \rightarrow OH(Ni) + OH(Ni)$	$6.373 \cdot 10^{+23}$	0.0	210.9	–
19	$O(Ni) + C(Ni) \rightarrow CO(Ni) + (Ni)$	$5.200 \cdot 10^{+23}$	0.0	148.1	–
20	$CO(Ni) + (Ni) \rightarrow O(Ni) + C(Ni)$	$1.354 \cdot 10^{+22}$	-3.0	116.1	-50.0 [c]
21	$O(Ni) + CO(Ni) \rightarrow CO_2(Ni) + (Ni)$	$2.000 \cdot 10^{+19}$	0.0	123.6	-50.0 [c]
22	$CO_2(Ni) + (Ni) \rightarrow O(Ni) + CO(Ni)$	$4.653 \cdot 10^{+23}$	-1.0	89.3	–
23	$HCO(Ni) + (Ni) \rightarrow CO(Ni) + H(Ni)$	$3.700 \cdot 10^{+21}$	0.0	0.0	50.0 [c]
24	$CO(Ni) + H(Ni) \rightarrow HCO(Ni) + (Ni)$	$4.019 \cdot 10^{+20}$	-1.0	132.2	–
25	$HCO(Ni) + (Ni) \rightarrow O(Ni) + CH(Ni)$	$3.700 \cdot 10^{+24}$	-3.0	95.8	–
26	$O(Ni) + CH(Ni) \rightarrow HCO(Ni) + (Ni)$	$4.604 \cdot 10^{+20}$	0.0	110.0	–
27	$CH_4(Ni) + (Ni) \rightarrow CH_3(Ni) + H(Ni)$	$3.700 \cdot 10^{+21}$	0.0	57.7	–
28	$CH_3(Ni) + H(Ni) \rightarrow CH_4(Ni) + (Ni)$	$6.034 \cdot 10^{+21}$	0.0	61.6	–
29	$CH_3(Ni) + (Ni) \rightarrow CH_2(Ni) + H(Ni)$	$3.700 \cdot 10^{+24}$	0.0	100.0	–
30	$CH_2(Ni) + H(Ni) \rightarrow CH_3(Ni) + (Ni)$	$1.293 \cdot 10^{+23}$	0.0	55.3	–
31	$CH_2(Ni) + (Ni) \rightarrow CH(Ni) + H(Ni)$	$3.700 \cdot 10^{+24}$	0.0	97.1	–
32	$CH(Ni) + H(Ni) \rightarrow CH_2(Ni) + (Ni)$	$4.089 \cdot 10^{+24}$	0.0	79.2	–
33	$CH(Ni) + (Ni) \rightarrow C(Ni) + H(Ni)$	$3.700 \cdot 10^{+21}$	0.0	18.8	–
34	$C(Ni) + H(Ni) \rightarrow CH(Ni) + (Ni)$	$4.562 \cdot 10^{+22}$	0.0	161.1	–
35	$O(Ni) + CH_4(Ni) \rightarrow CH_3(Ni) + OH(Ni)$	$1.700 \cdot 10^{+24}$	0.0	88.3	–
36	$CH_3(Ni) + OH(Ni) \rightarrow O(Ni) + CH_4(Ni)$	$9.876 \cdot 10^{+22}$	0.0	30.4	–
37	$O(Ni) + CH_3(Ni) \rightarrow CH_2(Ni) + OH(Ni)$	$3.700 \cdot 10^{+24}$	0.0	130.1	–
38	$CH_2(Ni) + OH(Ni) \rightarrow O(Ni) + CH_3(Ni)$	$4.607 \cdot 10^{+21}$	0.0	23.6	–
39	$O(Ni) + CH_2(Ni) \rightarrow CH(Ni) + OH(Ni)$	$3.700 \cdot 10^{+24}$	0.0	126.8	–
40	$CH(Ni) + OH(Ni) \rightarrow O(Ni) + CH_2(Ni)$	$1.457 \cdot 10^{+23}$	0.0	47.1	–
41	$O(Ni) + CH(Ni) \rightarrow C(Ni) + OH(Ni)$	$3.700 \cdot 10^{+21}$	0.0	48.1	–
42	$C(Ni) + OH(Ni) \rightarrow O(Ni) + CH(Ni)$	$1.625 \cdot 10^{+21}$	0.0	128.6	–

[a] Arrhenius parameters for the rate constants written in the form: $k = AT^n \exp(-E/RT)$. The units of A are given in terms of moles, centimeters, and seconds. E is in kJ mol^{-1}.
[b] Sticking coefficient.
[c] Coverage-dependent activation energy. Total available surface density Γ is expressed in mol cm^{-2} and represents the tuning parameter.

Chemkin to Cantera format. Valuable information about mechanism files were sourced from Dalle Nogare's work [26]. The mechanism is formulated in terms of elementary reactions occurring over the catalyst surface and the reaction rates depend both on the concentrations of gaseous reactants as well as on the coverage of those species representing reactive surface sites and adsorbates. The coverage is not known *a priori* and must to be determined as a part of the solution. The net production rate of any species (gas or surface) in reaction j is given by:

$$\dot{\omega}_k = \sum_j \nu_{k,j} q_j \tag{7}$$

where q_j is the rate of reaction j and $\nu_{k,j}$ is the net stoichiometric coefficient. The reaction rates for bulk species are computed assuming mass-action kinetics, with temperature-dependent rate coefficients in the Arrhenius form [9]:

$$k_i = A_i T^n \exp(-E_i/RT) \tag{8}$$

2.2. Modelling of heterogeneous reactions within the anode electrode

Thermal heterogeneous production rates are often evaluated using empirical correlations able to express the reaction rate for each species as a function of the local gas composition without considering intermediate heterogeneous reaction steps. However, most rate expressions come from experimental analysis and do not account for reverse reactions that become more and more important as the gas approaches the equilibrium condition. As a consequence, reversible potentials can be often affected by relevant errors. An improved approach instead consists of considering a set of reversible heterogeneous reactions and subsequently to compute reaction rates using mass-action kinetics. By doing this, reverse rates are evaluated consistently with thermodynamic laws. In particular, by choosing reactions and rates to fit experimental data, it becomes possible to represent measured reaction rates data under non-equilibrium condition, and to ensure that forward and reverse reactions balance each other as equilibrium is approached.

Nickel is the most common anode material (in Ni–YSZ cermets) and is also a well-known catalyst for industrial steam-reforming reactors. Hence, the reactions of methane on Ni have been extensively studied for decades, and different reaction mechanisms have been proposed and modelled so far.

The reaction mechanism given in Table 1, and used for this work, consists of a set of 42 irreversible reactions, with 6 gas-phase species and 12 additional adsorbed species. Most of the reaction rates are represented in the Arrhenius form or in term of a sticking coefficient. Heterogeneous reactions rates also depend on surface coverage of the involved species. As an example, the net reaction rates of reactions 12, 20, 21, and 23 depend on the carbon-monoxide coverage $\theta_{CO(s)}$ through the expression:

$$k = AT^n \exp\left(-\frac{E}{RT}\right) \exp\left(-\frac{\varepsilon_{CO(s)} \theta_{CO(s)}}{RT}\right) \tag{9}$$

Although the reaction mechanism is written as pairs of irreversible reactions, the reverse rate coefficients depend on the forward rate coefficients and thermodynamics. The reverse rate coefficients are computed indeed to ensure thermodynamic consistency and an asymptotic approach to the equilibrium state.

Elementary reaction mechanisms have a broader validity with respect to global mechanisms that generally can be used only under selected geometric configurations and operating conditions. The used mechanism was initially developed and validated using nickel-coated honeycomb monoliths for a temperature ranging from 700 to 1300 K. The mechanism has been recently validated for SOFC cermet anodes by Zhu et al. [13,14].

Since the reaction mechanism is based on elementary molecular processes, it represents all the chemical reactions occurring within the SOFC anode, including steam reforming of CH_4 to CO and H_2 and water–gas-shift.

2.3. Model solution

Input data of the model are: i) pressure and temperature data (the latter was assumed constant in the present model); ii) a detailed reaction mechanism; iii) the current load applied to the fuel cell (optionally a shape function for current profile can be also provided); iv) the fluxes of all chemical species entering the anode gas channel; and v) the cell geometric parameters (anode channel length, radius and thickness, number of cells for the axial and radial discretization). The discretization of the fuel cell domain is shown in Fig. 1.
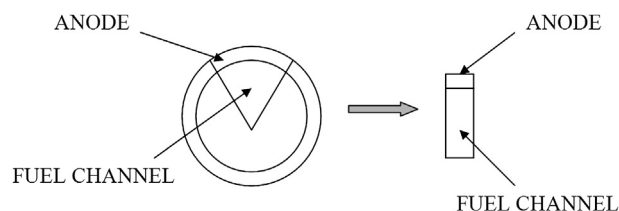
Fig. 1. Radial-wedge-to-rectangular-channel approximation.

The anode volume was approximated by an interface where all reactions and transport phenomena were collapsed over a surface. As the anode was considered as a reacting wall/surface, no account was taken for reacting and mass transport phenomena in the porous-electrode. Net production rates of all chemical species were computed directly from the mechanism file, while production and destruction rates due to the current applied to the fuel cell were computed according to the Faraday's law.

The fuel channel was divided into several elements along the axial direction and each of them was solved uni-dimensionally along the radial coordinate only. In this way, diffusive transport phenomena were assumed to be dominant with respect to convection. Convergence of the model was obtained iteratively.

3. Experimental

3.1. Single-cell test setup

Several operational conditions were tested on a tubular SOFC (Acumentrics, US) by varying current density, fuel utilization and anode gas composition. The cell used for the experiments was an anode-supported type with a Ni−YSZ anode, an 8YSZ electrolyte and LSM cathode. The tube was 331 mm long, with an inner diameter of 10.5 mm; the anode is ∼1700 μm thick; while electrolyte and cathode are 37 μm and 50 μm thick, respectively. The cell was designed with a triple current take-off (consisting of Ag wires) to limit ohmic losses associated with too long electronic paths for current collection.

The cell has been experimentally characterized in a test-stand specifically designed to operate as a platform for the evaluation of up to five single tubular cells. The test-stand incorporates all the equipment needed to feed fuel and oxidant gases, to control the cell operating temperature and finally to log data while the experiment is running. A detailed description of the test-rig used is found elsewhere [27].

An advantage of the tubular geometry over the planar is the straight separation of anode and cathode reactants/exhausts and

thus an easier evaluation of the thermal gradient inside the tube (i.e., the anode volume) with regard to the electrochemical and chemical reactions there occurring. In the bulk of the anode volume, along the longitudinal direction of the tube, three thermocouples were placed to measure the gas temperature (these were located at a distance of 140 mm, 260 mm and 320 mm, respectively, from the tube outlet section, as shown in Fig. 2). Five voltage measurements were taken along the fuel cell through five voltmeters. The voltage of the central voltmeter was taken as the voltage representative of cell performance [27].

The oven temperature was set at a temperature of 830 °C for all experiments in order to reach a cell temperature around 800 °C.

The anode off-gas stream was periodically collected and analyzed through a gas chromatographer (a "Thermo Finnigan" instrument equipped with a column of Porous Layer Open Tubular − PLOT, using Thermal Conductivity Detector − TCD and Argon as carrier gas). Gas analysis was used to evaluate at a macroscopic level the reactions taking place within the anode electrode and to validate the numerical model developed and described before.

In the SOFC tube assembly, a stainless steel (SS) cap plus tubing was sealed to the SOFC terminal end, using a ceramic cement. The SS pipe was eventually used to collect the anode off-gas.

The anode gas composition was always settled in order to avoid carbon-deposition on the anode: the addition of extra CO_2 (that added to the one already present in the biogas stream) was employed to promote a carbon-deposition-free dry-reforming [28]. The proper amount of CO_2 was pre-mixed with the biogas before the hot cell anodic compartment.

Tests with direct internal dry-reforming of biogas were performed by adding respectively 1.0, 1.5, and 2.0 (standard) mole of carbon dioxide per mole of biogas (corresponding to CO_2:CH_4 ratios of 2.33, 3.17, and 4.00, respectively). A detailed description of all experiments performed is given in Table 2. A wide range of current loads under different fuel flow rates were tested to produce performance maps of the fuel cell.

3.2. Main results

Fuel utilization maps (or efficiency maps) were obtained by acquiring data starting from a methane mass flow rate corresponding to current load of 7.5 A and an FU of 25% (this was the minimum flow rate achieved by the available mass flow controller). Fig. 3 points out the relation existing between the cell efficiency and the electrical power produced by the cell (the data have been normalized for confidentiality issues). Lines of the same colour connect operational points characterized by the same current load (which is indicated near the points having lower FU). Black lines,
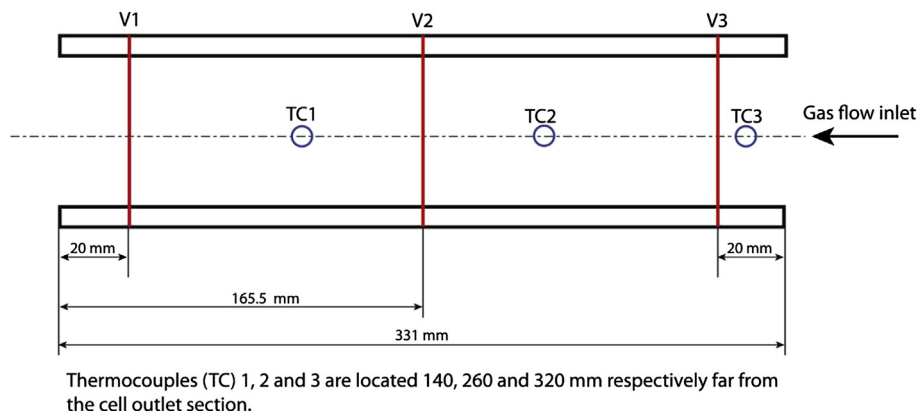

Thermocouples (TC) 1, 2 and 3 are located 140, 260 and 320 mm respectively far from the cell outlet section.

Fig. 2. Thermocouples and voltmeters positions inside the cell.

Table 2
Dry-reforming tests. Matrix design variable is methane flow rate (Nml min^{-1}), cell temperature is 800 °C, and CO_2 addition is set to 1.0, 1.5, and 2.0, respectively.

Current (A)	Fuel utilization													
	25%	30%	35%	40%	45%	50%	55%	60%	65%	70%	75%	80%	85%	90%
OCV	–	–	–	–	–	–	–	–	–	–	–	–	–	–
2.5	–	–	–	–	–	–	–	–	–	–	–	–	–	–
5	–	–	–	–	–	–	–	–	–	–	–	–	–	–
7.5	53	44	–	–	–	–	–	–	–	–	–	–	–	–
10	71	59	50	44	–	–	–	–	–	–	–	–	–	–
12.5	88	74	63	55	49	44	–	–	–	–	–	–	–	–
15	106	88	76	66	59	53	48	44	–	–	–	–	–	–
17.5	124	103	88	77	69	62	56	51	48	44	–	–	–	–
20	141	118	101	88	78	71	64	59	54	50	47	44	–	–
22.5	159	132	113	99	88	79	72	66	61	57	53	50	47	44
25	177	147	126	110	98	88	80	74	68	63	59	55	52	49

generally presenting a slight negative slope, combine points with the same *FU*.

In Fig. 3(a), the maximum efficiency (on an LHV basis), which is 43.4%, is achieved when *FU* is 70%. In Fig. 3(b), where the ratio is equal to 1.5, the maximum efficiency is 39.4% at an *FU* of 70%. In Fig. 3(c), where the ratio is equal to 2.0, the maximum efficiency is 36.8% at an *FU* of 60%. By analyzing the three maps together, it is clear again how dry-reforming is more effective for carbon dioxide-to-biogas ratios which are close to unity.

4. Model validation

The (dry) anode outlet gas composition was measured using a gas chromatograph with the fuel cell either operating at open circuit voltage (OCV) condition or under load. As mentioned earlier, the cell was tested under different CO_2:biogas molar ratios that were safe in term of carbon-deposition (CO_2:CH_4 ratios were 2.33, 3.17, and 4, respectively).

The model described above was used to obtain the gas composition profile along the fuel channel. The calculated outlet gas composition was compared with the measured one. For OCV only, the outlet gas composition was also evaluated using the software CEA [29] that gives the compositions at equilibrium.

Fig. 4 gives a comparison among the measured outlet gas composition, those obtained by the kinetic model and finally the equilibrium ones. No current load is applied to the cell (OCV configuration) and the CH_4 mass flow rate is set to 50 Nml min^{-1}. CO_2/biogas ratios are 1.0, 1.5, and 2.0 for Fig. 4(a)–(c), respectively.

In the kinetic model, to get a better match between the experimental data and the model results, the number of radial cells was set to 8, while the number of axial cells was set to 50 (convergence is reached very quickly and relative errors in mole-fractions evaluation are already lower than 1% when using 25–30 axial cells). The Ni catalyst surface site density was set to $25.00 \cdot 10^{-9}$ mol cm^{-2}. This value is quite high if compared to what generally reported in the literature that is $2.60 \cdot 10^{-9}$ mol cm^{-2} [13,14,25]. However, this is the only characteristic parameter of the fuel cell and it strongly depends on the Ni crystalline structure in the anode electrode and more generally on the morphology of the anode itself. Note that mentioned literature studies [13,14] refer to a planar SOFC, manufactured differently from tubular cells and thus with different microscopic features.

Measured hydrogen and carbon-monoxide concentrations are lower than the corresponding equilibrium concentrations, while carbon dioxide production is higher. The CH_4 concentration predicted by the kinetic model (not reported in the graphs) is around 3% for all the three CO_2/biogas ratios; while water concentration is around 2% (Note that concentrations in the graphs were always normalized to produce a dry-basis comparison.). The match between the kinetic model and experimental results is only fairly good. In the measured gas samples, a relatively high content of N_2 was always found (8.76% for data in Fig. 4(a), 8.86% for Fig. 4(b), and 4.95% for Fig. 4(c)), probably due to air infiltration. If air enters the fuel channel and no oxygen is found in the final composition, this means that O_2 is free to react inside the channel and combustion reactions are likely to occur. This could explain why no methane is ever found in the measured outlet compositions (even though a small fraction of un-converted of it was predicted by the kinetic model) and actual hydrogen concentration is always lower than the predicted one.

Fig. 5 gives a comparison between the kinetic model and the measured data when the cell was operated at 15 A and *FU* of 50%.

Differently from the OCV cases, the trend of the dry-gas composition largely varies according to the CO_2/biogas ratio selected; only the H_2 concentration is considerably higher than the experimental one for all cases.

Fig. 6 shows the comparison between model and experimental results when varying *FU* and current load. Fig. 6(a) shows what happens when the CO_2/biogas ratio is set to 1.5, the current load is 25 A and *FU* is 50% (corresponding to a CH_4 mass flow rate of 88 Nml min^{-1}). On the other hand, Fig. 6(b) shows the exhaust composition when the CO_2/biogas ratio was set to 1.5, the current load is 15 A and *FU* is 25% (corresponding to a CH_4 mass flow rate of 106 Nml min^{-1}).

The match between model and experimental results is very good for CO_2, fair for H_2 (with 5 percent points as the maximum discrepancy between model and measured data), while there is a quite pronounced mismatch for CO. The CH_4 final content is 3.0% and 5.6%, respectively, while water production (due to electrochemical reaction) leads to concentrations of 14.9% and 6.9%, respectively. Since N_2 mole fractions (2.32% and 2.50%, respectively) are quite low, and considering the relatively high water content for both cases, we can state that the discrepancies in the H_2 and CO mole fractions are probably due to the general tendency of the mechanism file to encourage water gas-shift over dry-reforming and steam-reforming processes, so that CO in the presence of water is mostly converted into CO_2.

Fig. 7 gives the predicted volumetric gas composition profiles of main anodic gases along the fuel channel for two different inlet composition and with the cell at OCV condition. The CH_4 flow rate is 50 Nml min^{-1}, while CO_2:biogas ratio is set 1.0 and 1.5, respectively.

For both cases, CH_4 (and consequently CO_2) are rapidly consumed to produce H_2 and CO. Also, a small amount of water is produced, probably due to reverse water gas-shift reaction. With both fuel compositions, chemical equilibrium is approached but never fully achieved. Dry-reforming reactions seems to proceed quickly in the first half of the fuel channel.
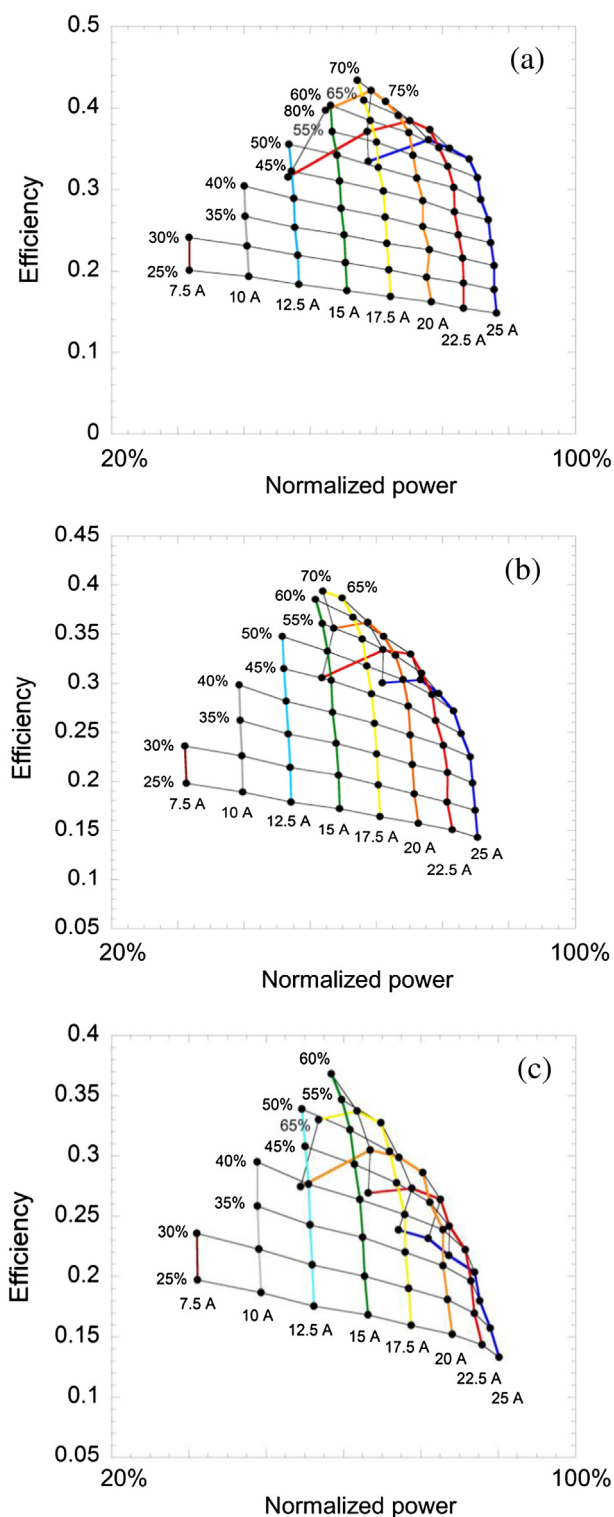
Fig. 3. Efficiency map with a carbon dioxide-to-biogas vol. ratio of (a) 1.0, (b) 1.5, (c) 2.0, respectively.
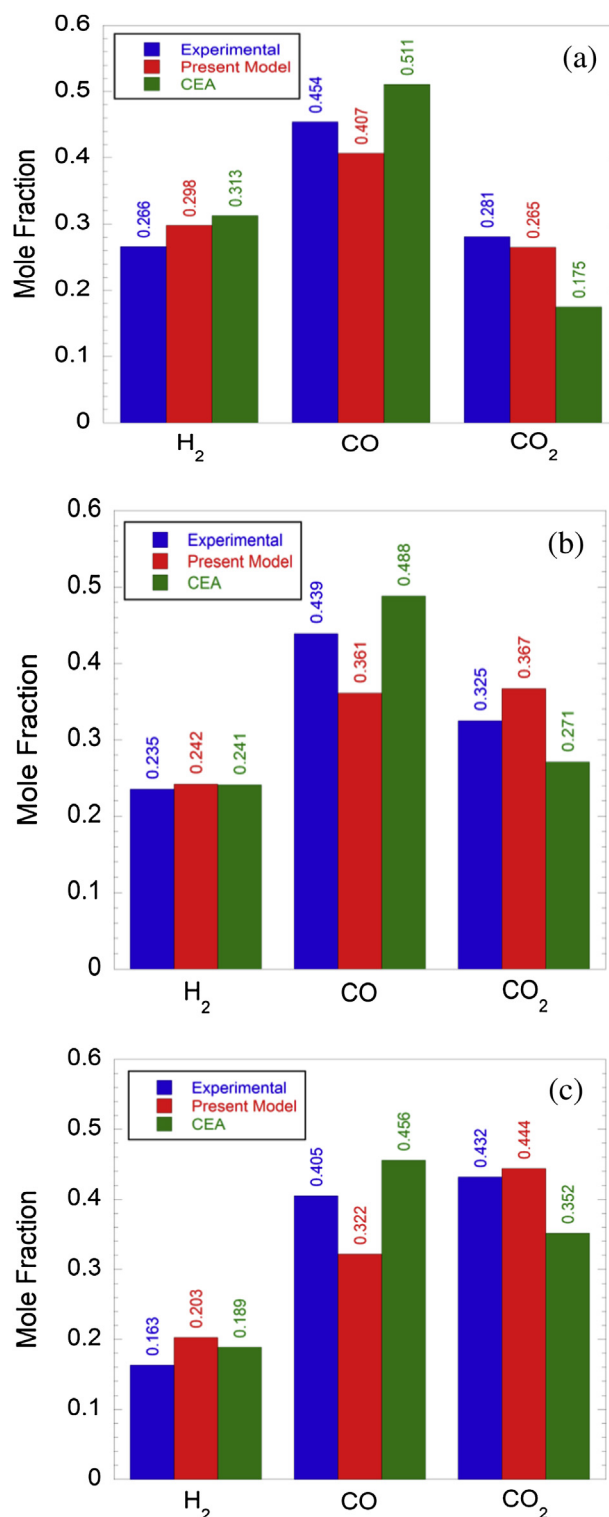

Fig. 4. Mole-fraction comparison (OCV configuration) for main dry-gas species when CO_2/biogas ratio is set to (a) 1.0, (b) 1.5, (c) 2.0, respectively.

Fig. 8 shows the predicted volumetric fraction profiles of main chemical species along the fuel channel when a current load of 15 A is applied to the cell. The CH_4 flow rate is 53 Nml min^{-1} (yielding an *FU* of 50%), while the CO_2:biogas ratio is equal to 1.0.

In this case, a quite large amount of water was produced because of the electrochemical reaction. This is the reason why CO is slightly consumed in the last part of the cell, in order to form CO_2 when

reacting with water (whose trend remains monotone because of its continuous electrochemical production).

5. Sensitivity analyses

A sensitivity analysis to selected variables of the proposed kinetic model was investigated looking at their influence on the
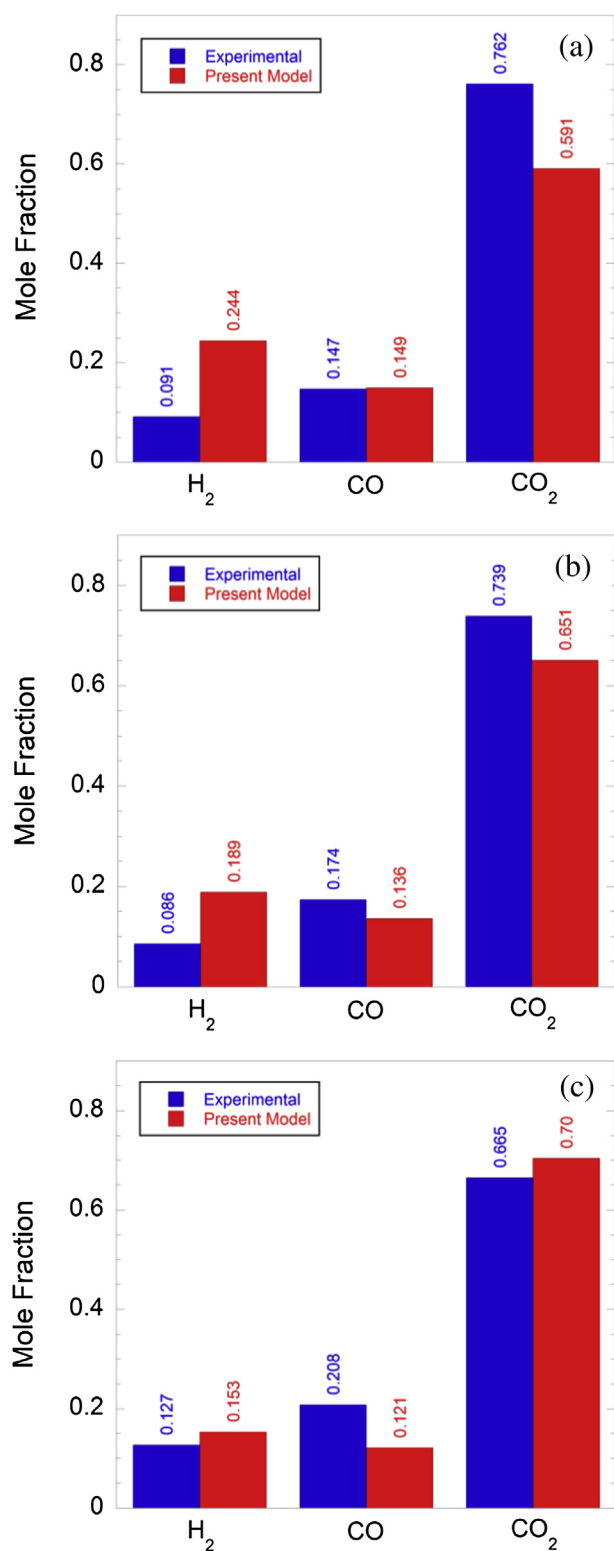
Fig. 5. Mole-fraction comparison ($I = 15$ A, $FU = 50\%$ configuration) for main dry-gas species when carbon CO_2/biogas ratio is set to (a) 1.0, (b) 1.5, (c) 2.0, respectively.

Fig. 6. Mole-fraction comparison for main dry-gas species when CO_2/biogas ratio is set to 1.5 when the configuration is set to (a) $I = 25$ A, $FU = 50\%$, (b) $I = 15$ A, $FU = 25\%$, respectively.

performance of the tubular SOFC. The following operating parameters were varied: the cell temperature, the inlet fuel composition, and the type of reforming process. In particular, the numerical kinetic model presented in this study was used to predict the effectiveness of steam reforming when both the cell temperature and the composition of the biogas mixture are varied.
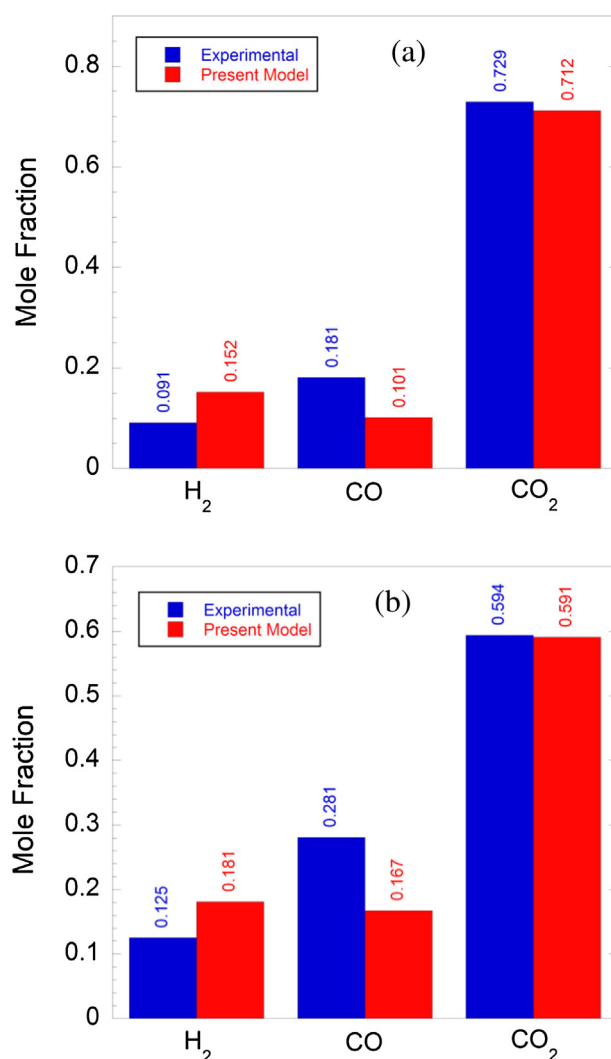
Even though the nominal temperature for the tubular SOFC here studied is $\sim$800 °C, the trend for market-ready SOFC-based generators points towards a reduction of the operating temperature; therefore, operation at lower temperature (in particular, 700 °C and 750 °C, respectively) was simulated. In the same way, the effectiveness of the reforming process occurring inside the cell was evaluated by changing the fuel anode composition. Table 3 presents the simplified composition (expressed in volume terms) of three different types of simulated biogas mixtures, i.e., the baseline biogas composition used for this work, a CO_2—lean biogas, and a so-called CO_2—purified methane (bio-methane).

Table 4 shows the composition of the biogas/water mixtures entering the anode channel in order to avoid carbon-deposition phenomena for all simulated biogases (Table 3) for different temperatures of the fuel cell.

Either the H_2O/biogas or the H_2O/CH_4 ratio may be easily specified as an input parameter of the present model by adding water in the input gas composition.

Table 5 gives the anode off-gas outlet composition for all the fuels considered, for different fuel cell operating temperatures. For each simulated case-study, OCV condition holds and the CH_4 flow rate is set to 50 Nml min^{-1}. Also, the number of radial and axial cells
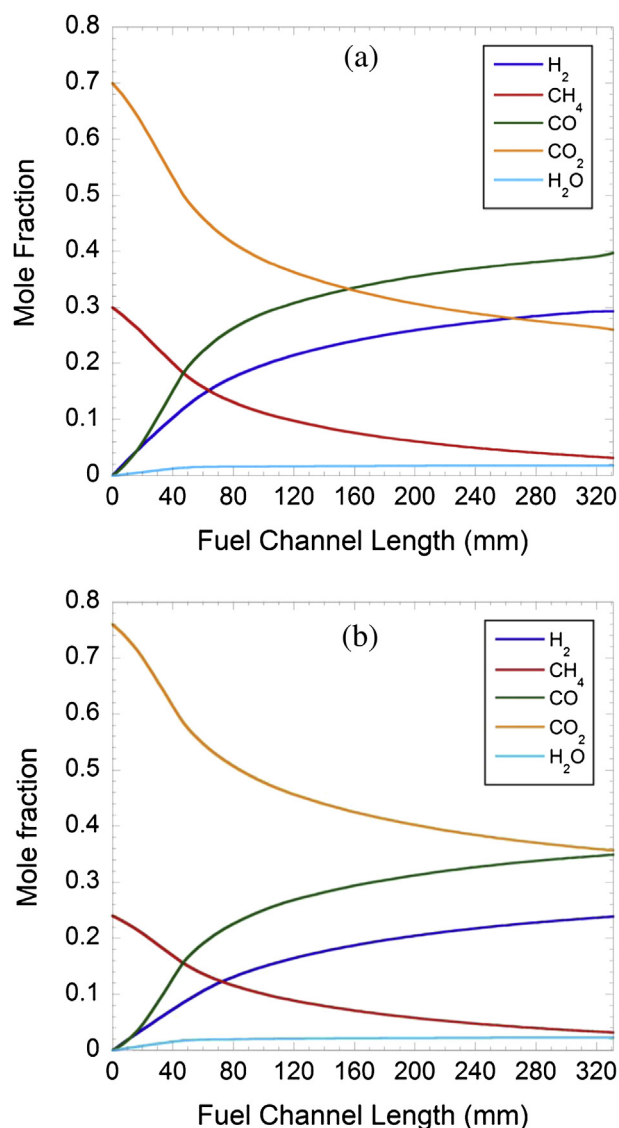
Fig. 7. Predicted mole-fraction profiles of main chemical species (OCV configuration) when CO_2/biogas ratio is set to (a) 1.0, (b) 1.5, respectively.

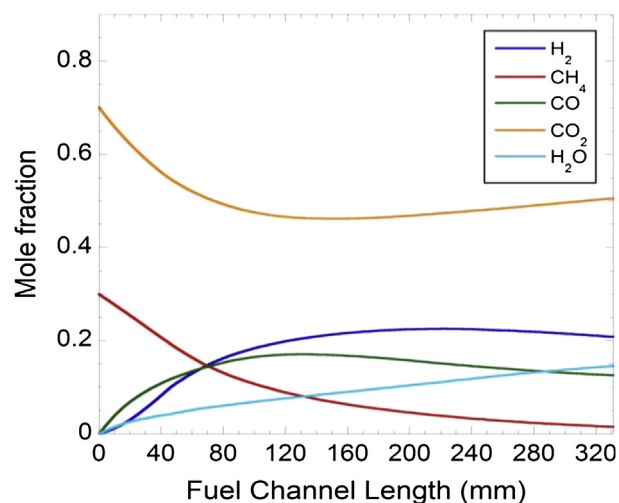**Fig. 8.** Predicted mole-fraction profiles of main chemical species when CO_2/biogas ratio is set to 1.0 ($I = 15$ A, $FU = 50\%$).

Table 3
Volumetric compositions for different type of simulated biogas mixtures.

Chemical species	Ref. biogas	Lean biogas	Bio-methane
CH_4 (%)	60	40	95
CO_2 (%)	40	60	5

Table 4
H_2O/biogas and H_2O/CH_4 ratios needed to avoid carbon-deposition with steam-reforming of different simulated biogas mixtures at different cell temperatures.

T (°C)	Ref. biogas		Lean biogas		Bio-methane	
	H_2O/BIO	H_2O/CH_4	H_2O/BIO	H_2O/CH_4	H_2O/BIO	H_2O/CH_4
800	0.28	0.47	0.19	0.48	0.93	0.98
750	0.37	0.62	0.01	0.03	0.99	1.04
700	0.54	0.90	0.00	0.00	1.11	1.16

is set to 8 and 50, respectively, while the surface site density is fixed and set to a value of 25×10^{-9} mol cm^{-2}. The cell temperature is set at 800 °C, 750 °C, and 700 °C, respectively.

Clearly, the lower the CO_2 concentration in the anode feed, the higher will be the H_2 concentration in the anode mixture. When varying the cell temperature, dry-reforming seems to be less effective. However, this effect is mainly due to the higher water content in the initial biogas/water mixture (see Table 4) required to avoid carbon-deposition.

In addition, for each fuel considered, the reforming process gets more effective in terms of H_2 production as the initial water content is increased, thus showing the higher effectiveness of steam reforming over dry-reforming. As expected, by lowering the fuel cell operating temperature, the amount of un-converted CH_4 found in the exhaust increases, as a consequence of the lower catalytic activity of Ni.

In particular, both the reference biogas mixture and bio-methane present linear trends, while lean biogas seems to show quite inconsistent results, but this is simply due to the absence of water in the initial composition when the cell temperature is set to 800 °C and 750 °C (see Table 4), with steam reforming being nearly or totally absent.

Eventually, Table 6 shows the final composition of the outlet stream for all biogases when the cell temperature is set to 800 °C and the current applied to the cell is 15 A. CH_4 mass flow rate is conventionally set to 50 Nml min^{-1} again ($FU = 53\%$). All considerations made above stay valid. Furthermore, here it is clear how a considerably large amount of water is electrochemically produced

Table 5
Simulated exhaust-gas composition in OCV configuration when steam reforming is performed for reference biogas (60% CH_4, 40% CO_2), lean biogas (40% CH_4, 60% CO_2) and bio-methane (95% CH_4, 5% CO_2) at different cell temperatures.

Reference biogas (60% CH_4, 40% CO_2) + safety H_2O					
T (°C)	H_2	H_2O	CH_4	CO	CO_2
800	55.60%	0.40%	2.78%	35.71%	5.51%
750	56.03%	1.04%	4.05%	28.98%	9.91%
700	56.86%	2.31%	4.72%	20.96%	15.15%
Lean biogas (40% CH_4, 60% CO_2) + safety H_2O					
T (°C)	H_2	H_2O	CH_4	CO	CO_2
800	37.35%	0.88%	3.93%	43.30%	14.54%
750	34.90%	0.83%	5.79%	41.21%	17.27%
700	41.73%	2.39%	5.53%	25.64%	24.71%
Bio-methane (95% CH_4, 5% CO_2) + safety H_2O					
T (°C)	63.73%	0.16%	2.30%	30.61%	3.20%
800	63.98%	0.42%	3.26%	29.06%	5.10%
750	64.30%	1.22%	4.56%	21.37%	8.54%
700	63.73%	0.16%	2.30%	30.61%	3.20%

Table 6
Simulated anode off-gas composition with steam-reforming of reference biogas, CO_2—lean biogas, and methane (the cell temperature is set to 800 °C with a current load of 15 A).

Fuel	H_2 (%)	H_2O (%)	CH_4 (%)	CO (%)	CO_2 (%)
Ref. biogas	34.67	23.85	1.40	6.84	33.25
Lean biogas	26.24	21.17	1.56	7.97	43.07
Bio-methane	40.00	33.47	0.93	3.59	22.01

and is available to take part in the reactions, with steam reforming being kinetically faster than dry-reforming. The main effect is the rise of CO_2 production, with CO final emissions being consequently lower.

6. Conclusions

A mathematical model of a tubular fuel cell, including heterogeneous catalysis in the fuel anode volume and electrochemical reactions operating on direct internal reforming of biogas was developed. The model capability to predict the volumetric gas composition along the anode channel was validated by comparing the measured gas composition of the anode exhaust stream with the one obtained by the numerical simulations. Interestingly, the model results confirmed that thermodynamic-equilibrium conditions are not fully achieved inside the anode channel and thus at the anode outlet section. However, the experimental results — that include a wide range of operating conditions — suggest that a direct biogas utilization in an anode-supported SOFC provides good performance and also ensures a good conversion of the methane fuel. In particular, experimental sessions with dry-reforming of biogas and with CO_2-lean to CO_2-rich conditions have been evaluated, obtaining efficiency maps of the fuel cell. The influence of the $CO_2:CH_4$ vol. ratio has been studied, with best efficiency being achieved for a ratio set to unity.

Finally, a sensitivity analysis has been performed using the validated model to investigate the influence of selected variables on the behavior of the tubular SOFC. The following variables have been selected: the cell temperature, the composition of the fuel entering the cell, and the typology of the reforming process (i.e., steam- vs. dry-reforming). The final composition of the outlet stream for all cases (reference biogas, lean biogas, and bio-methane, respectively), in case of direct biogas steam reforming when different temperatures are applied to the tubular SOFC, are predicted by the model. In OCV condition, the reforming process gets more effective in case of bio-methane (higher H_2 mole fractions, CO_2 emissions lower than 10%, lower CO contents and lowest content of residual CH_4 and H_2O). Also, for each fuel, the reforming process gets more effective as the initial water content is increased, thus showing a good effectiveness of steam reforming even though the cell temperature is far away from the nominal value.

Acknowledgments

Nomenclature

Greek symbols
ρ density (kg m^{-3})
μ dynamic viscosity (Pa s)

λ thermal conductivity (W m^{-1} K^{-1})
Λ constant
$\dot{\omega}$ molar net production rate (mol m^{-2} s^{-1})
ν net stoichiometric coefficient
$\varepsilon_{CO(s)}$ coverage-dependent activation energy (J)

Symbols
A Arrhenius pre-factor (A m^{-2})
c_p specific heat capacity at constant pressure (J kg^{-1} K^{-1})
E activation energy (J)
F Faraday constant (C mol^{-1})
h specific enthalpy (J kg^{-1})
i current density (A m^{-2})
J molar flux (mol m^{-2} s^{-1})
K_s number of surface species
P pressure (Pa)
P_0 reference pressure (Pa)
r radial coordinate (m)
t time (s)
T temperature (K)
u axial velocity (m s^{-1})
v radial velocity (m s^{-1})
V normalized radial velocity (s^{-1})
W molecular weight (kg kmol^{-1})
X mole fraction
Y mass fraction
z axial coordinate (m)

Indices
a anodic side
i reaction
j, k, m species
surf   surface species

Acronyms
FU   fuel utilization
LHV   low heating value
OCV   open circuit voltage
SOFC   solid oxide fuel cell

References

[1] L. Appels, J. Baeyens, J. Degrève, R. Dewil, Progress in Energy and Combustion Science 34 (6) (2008) 755—781.
[2] R. Dewil, L. Appels, J. Baeyens, Energy Conversion and Management 47 (2006) 1711—1722.
[3] EPRI, Assessment of Fuel Gas Cleanup Systems for Waste Gas Fueled Power Generation. Electric Power Research Institute 1012763 Technical Update, 2006, p. 117.
[4] M. Arnold, Reduction and Monitoring of Biogas Trace Compounds. VTT Research Notes 2496 VTT, Espoo. 74 pp. + app. 5 (2009) (last accessed on May 26th, 2012), http://www.vtt.fi/inf/pdf/tiedotteet/2009/T2496.pdf.
[5] M. Arnold, T. Kajolinna, Waste Management 30 (6) (2010) 1011—1017.
[6] Y. Shiratori, T. Oshima, K. Sasaki, International Journal of Hydrogen Energy 33 (2008) 6316—6321.
[7] Y. Takahashi, Y. Shiratori, S. Furuta, K. Sasaki, Solid State Ionics 225 (2012) 113—117.
[8] Y. Shiratori, T. Ijichi, T. Oshima, K. Sasaki, International Journal of Hydrogen Energy 35 (2010) 7905—7910.
[9] A. Lanzini, P. Leone, International Journal of Hydrogen Energy 35 (2010) 2463—2476.
[10] M. Vogler, A. Bieberle-Hutter, L. Gauckler, J. Warnatz, W.G. Bessler, Journal of the Electrochemical Society 156 (5) (2009) B663—B672.
[11] Y. Hao, D.G. Goodwin, Journal of the Electrochemical Society 155 (7) (2008) B666—B674.
[12] D.G. Goodwin, H. Zhu, A.M. Colclasure, R.J. Kee, Journal of the Electrochemical Society 156 (9) (2009) B1004—B1021.
[13] H. Zhu, R.J. Kee, V.M. Janardhanan, O. Deutschmann, D.G. Goodwin, Journal of the Electrochemical Society 152 (12) (2005) A2427—A2440.
[14] E.S. Hecht, G.K. Gupta, H. Zhu, A.M. Dean, R.J. Kee, L. Maier, O. Deutschmann, Applied Catalysis A: General 295 (2005) 40—51.

[15] Y. Hao, D.G. Goodwin, Journal of the Electrochemical Society 154 (2) (2007) B207–B217.
[16] Y. Jiang, A.V. Virkar, Journal of the Electrochemical Society 150 (2003) A942–A951.
[17] V. Yurkiv, D. Starukhin, H.-R. Volpp, W.G. Bessler, Journal of the Electrochemical Society 158 (2011) B5–B10.
[18] C.J. Moyer, N.P. Sullivan, H. Zhu, R.J. Kee, Journal of the Electrochemical Society 158 (2011) B117–B131.
[19] C. Li, Y. Shi, N. Cai, Journal of Power Sources 195 (8) (2010) 2266–2282.
[20] Y. Shi, C. Li, N. Cai, Journal of Power Sources 196 (13) (2011) 5526–5537.
[21] Y. Shi, N. Cai, C. Li, Journal of Power Sources 164 (2) (2007) 639–648.
[22] Cantera 2.0, "Chemical Kinetics, Thermodynamics and Transport Process", http://cantera.github.com/docs/sphinx/html/index.html, (last accessed on May 27th, 2012).
[23] J.O. Hirschfelder, C.F. Curtiss, R.B. Bird, Molecular Theory of Gases and Liquids, John Wiley and Sons, New York, 1954.
[24] T.P. Coffee, J.M. Heimerl, Combustion and Flame 43 (1981) 273.
[25] http://www.detchem.com.
[26] D. Dalle Nogare, Modeling Catalytic Methane Partial Oxidation with Detailed Chemistry. PhD Thesis, Dipartimento dei Principi e Impianti dell'Ingegneria Chimica "I. Sorgato", Università degli Studi di Padova, 2008.
[27] A. Lanzini, P. Leone, M. Pieroni, M. Santarelli, D. Beretta, S. Ginocchio, Fuel Cells 11 (2011) 697–710.
[28] A. Lanzini, P. Leone, C. Guerra, F. Smeacetto, N.P. Brandon, M. Santarelli, International Journal of Hydrogen Energy (2012).
[29] S. Gordon, B.J. McBride, Computer Program for Calculation of Complex Chemical Equilibrium Compositions and Applications, NASA, 1996.